Flow Control Applied to the Front Rounded Edge of a Bluff Body

Lubinsky Gad and Seifert Avraham
School of Mechanical Engineering, Faculty of Engineering, Tel Aviv University
Tel Aviv 69978, ISRAEL

Abstract
An experimental study was performed on a 2D square prism with one rounded front edge with the purpose of reducing the aerodynamic drag by means of active flow control of boundary layer separation. Highly efficient suction and oscillatory blowing (SaOB) actuators were installed at the front curved edge, aimed to inhibit the separation phenomenon. The experimental results show significant decrease in the form-drag, narrowing of the wake and correspondingly an increase in the base pressure in the presence of the SaOB actuation. The mechanism of drag reduction is elimination of the separation from the front-cured edge of the model.

NOMENCLATURE

AFC	Active Flow Control
AFM 4	Energy Figure of Merit
C_{df}	Front-side drag coefficient
C_{dp}	Pressure drag coefficient
C_l	Lift coefficient
C_p	Pressure coefficient
$-C_{pb}$	Averaged base pressure coefficient (Inverted)
C_μ	Momentum coefficient
d	Wake width for threshold definition of 0.7 U_∞
f	Vortex shedding (dominant) frequency
H	Model height and length
h	Pulsed Blowing Slot (PBS) width
R	cylinder radius
Re	Reynolds number based on 2R
SaOB	Suction and Oscillatory Blowing
St	Strouhal number based on 2R
St^*	Strouhal number based on the wake width
TAU	Tel-Aviv University
U_∞	Free-stream velocity
u_b	Mean pulsed blowing velocity
x	Horizontal component, Free-Stream direction
y	Vertical component
α	Angle of Attack
θ	Upper AFC cylinder Pulsed blowing location (angle)

1. INTRODUCTION

The need to reduce the fuel consumption of road vehicles, in particular of heavy ones, is an important scientific and technological challenge, due to its economic, environmental and political impact. The US fuel consumption of heavy vehicles is growing and expected to exceed 25% of the total consumption of the transportation sector by 2040[1]. One of the reasons for the high fuel consumption is the aerodynamic drag which is a major component of the total energy invested to drive a large vehicle. About third to half of the engine power is invested in overcoming the aerodynamic drag at highway speeds [1].

For large commercial vehicles, the most important design guideline is maximum storage volume. Therefore, unlike passenger cars, these vehicles are designed as box shaped bluff-body. Bluff-body is

characterized by a large region of separated flow and high form-drag resulting from low pressure at its rear surface and near wake. Nevertheless, not all the challenges are at the rear-of the vehicle. The flow could separate from the vehicle's surface just downstream of its frontal face, also resulting in in drag increase. The traditional way for minimizing the drag force acting on the vehicle, resulting from its large cross-section area, is to assure a large enough radius of the front side corners in order to prevent boundary layer separation. Therefore, the front windows should be curved in multiple planes and form a smooth transition between the body and window sections [1, 2]. There are three main reasons that render designing sufficiently large corner radii around this region (termed A-pillar) problematic. First, for manufacturing considerations, it is very difficult to mount a small radius windscreen. Second, for visibility reasons, small radius of curvature glass can cause distortions. Third, there is a legal requirement of how far out to the sides the windscreen should be wiped, something which is impossible to fulfill if the windscreen is highly curved. As a result, current design methodology significantly limits the functionality of the vehicle, limiting the field of view and reducing the internal volume of the cab and installed systems. Reducing the turning radius of the front window edges, will solve the functionality issues but would lead to flow separation at these regions and to significant increase in aerodynamic drag and fuel consumption. A suitable solution for these contradicting requirements could be achieved by the use of Active Flow Control (AFC). AFC technology is capable of preventing separation of the flow by the use of actuators in a highly energy efficient manner [3]. Therefore, the use of AFC will relax one of the stringent design constraints that currently prevail.

For the current application, the TAU developed SaOB (Suction and Oscillatory Blowing) actuator, which was proven to be a valuable and efficient tool for boundary layer separation control, was installed at the front-upper-edge of a 2D bluff-body model. This actuator combines both steady suction and pulsed blowing, in close proximity and has no moving parts. The suction effect is created by an ejector fed with compressed air and the oscillatory blowing is created by a bi-stable fluidic oscillator which is fed by a mixture of the air inhaled from the outer flow and the inlet air pressure supply [4-8]. This paper presents the aerodynamic effects of flow control applied to a square prism with one rounded front corner using an array of SaOB actuators located at the front- rounded edge of the body.

The structure of the remaining parts of the paper is as follows: The experimental set-up is discussed in chapter 2.The experimental findings are presented and discussed in Chapter 3 to be followed by discussion and summary in sec. 4.

2. EXPERIMENTAL SETUP

Experiments were carried out in the Knapp-Meadow low-speed closed-loop wind tunnel. The test section dimensions are 609 mm (width) by 1500 mm (height) by 4250 mm (length). The turbulence level in the tunnel is 0.1 to 0.2%, slightly increasing with the tunnel speed (which is between 3 m/s and 65 m/s). The tunnel free-stream velocity and temperature were constantly monitored and controlled, with lower than 1% uncertainty in speed and better than 1˚C in temperature.

A 2D generic cab model was designed (Fig. 1). The model spans the 609 mm width of the test section. Its cross-section is a square with H=300 mm length. The model is located 1200 mm from the test section entrance and its upper surface is 690 mm below the tunnel ceiling. The wind tunnel model and its cross-section are shown in Figure. 1. Unless otherwise stated, the model incidence angle is set at zero degrees (±0.2˚), i.e., it aligns with the free-stream velocity direction, simulating no cross-wind situation.

A circular cylinder with radius of R=38.1 mm functions as the upper forward corner of the model, as shown in Fig. 1b. Inside the cylinder, 7 AFC SaOB actuators (synchronized in a π phase lag) are installed [7] .The SaOB actuator and the array of actuators inside the cylinder are shown in Figure 2. A Pulsed Blowing Slot (PBS), 2 mm wide, enables the actuators' pulsed blowing jet to interact with the external flow. The pulsed blowing and suction velocities were based on calibration data acquired by an Hot Wire (HW) measurements [7, with relevant uncertainty information provided there]. Over the entire span of the cylinder 96 holes of 2 mm diameter were drilled for suction. The suction holes are located 15˚ upstream of the PBS. In [7] and references therein, it was shown that suction can delay separation in most relevant cases and with magnitude up to half the free-stream velocity by 15˚. The cylinder can rotate around its axis moving the suction holes and the PBS independently of the angle of attack of the model. The PBS angle (θ) is defined as the angle between the free-stream velocity (U_∞) and the PBS location, with 90˚ being the cylinder summit, which coincides with the front edge of the flat upper model surface (Figure 1b). The uncertainty of θ is 0.2˚.

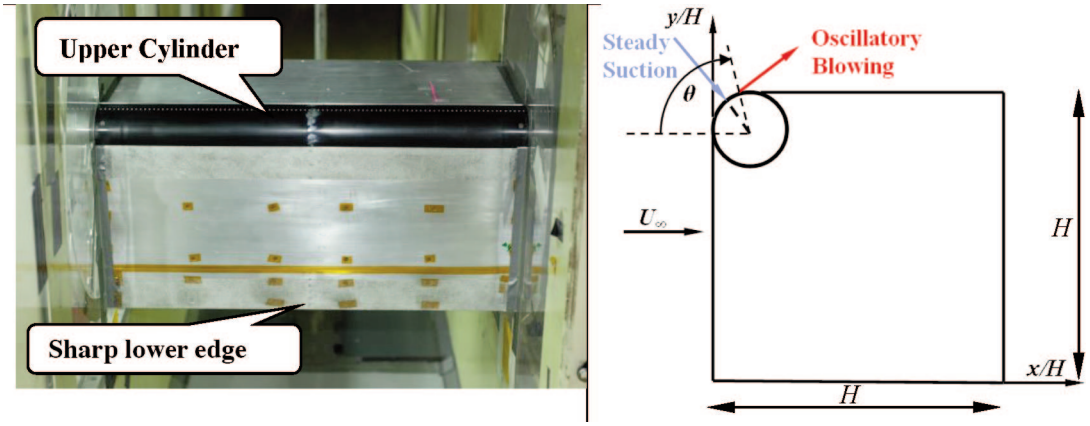

(a) (b)

Figure 1. (a) The model installed in the Knapp-Meadow wind tunnel. (b) A cross-section of the 2D generic cab model, H=300 mm, cylinder diameter is 2R=76.2 mm.

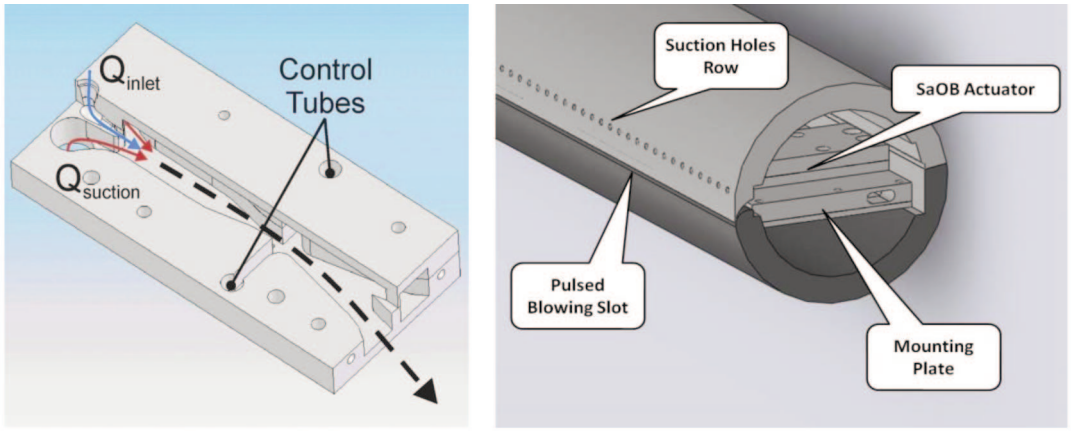

(a) (b)

Figure 2. (a) The SaOB actuator cross-section [4]. (b) An array of 7 SaOB actuators installed inside the cylinder model [7] that is used at the upper-frond edge of the square prism model for AFC. The suction holes and the pulsed blowing slot (PBS) are shown as well. External flow over the cylinder at this orientation will be from top to bottom.

At the mid span position of the model, 65 pressure taps are located, with smaller spacing near the model's corners. Additionally, the rotating cylinder has 46 pressure taps with increments of 7.5°. The pressure taps locations could be described by the horizontal and vertical axes shown in Figure 1b. Additionally, the pressure tap locations around the upper-front curved edge can be described either by the angle with respect to the free-stream direction: θ' is the angle between the free-stream to the pressure tap of the upper FC cylinder.

A wake rake is located about 900 mm downstream of the rear (lee-side) end of the model. It includes 60 ports on a vertical traverse system. The model surface pressures, the wake total pressures and the Pitot tube which measure the free-stream pressure were acquired by a PSI^{TM} ESP-8400 pressure scanner. Its full scale is either 1 PSI or 10"H2O and an uncertainty of 0.1% of the full-scale (at the minRe = 550 imum tested speed). Three unsteady pressure sensors (Endevco) were installed to measure unsteady effects. One sensor was connected to the middle actuator control port for measuring the oscillations frequency (termed "Feedback"). Another sensor was placed on the wake rake, at a vertical distance of 140 mm above the upper surface of the model. The last sensor was placed on the upper surface of the model close to the rear surface (x/H=0.96, y/H=1). All the unsteady pressure sensors could provide information about unsteady effects, including periodic separation and the vortex

shedding phenomenon resulting from it. The frequency resolution is better than 0.1Hz while the frequency response as installed is flat over the entire relevant range (0-500Hz).

Tests were conducted over a range of Reynolds numbers, between $0.2x10^6$ and $0.5\ x10^6$, based on the model height. Baseline measurements were carried out, including taping over the PBS and the suction holes, using an adhesive Kapton tape, 19 mm width and 0.05 mm thick.

In order to examine the model performance in transitional and turbulent flow, the front side of the model was covered by a double sided adhesive tape, 0.1 mm thick, sparsely covered by Alumina powder with grain size k/H = 0.0005 (Grit #60). AFC tests were performed with the rough front configuration using a range of magnitudes and θ (PBS locations). Again, suction is applied 15 degrees upstream of the PBS location. Due to the significant blockage of the tunnel by the model (20%), the sensitivity to Reynolds number of the transition and the separation process and other secondary effects, such as 3D effects, it is difficult to quantify the absolute uncertainty of the drag measurements. However, for a given Reynolds number and AFC location, baseline data, with and without tape covering the AFC openings were always acquired. Then a series of AFC magnitude tests were conducted. These tests are estimated to be repeatable with uncertainty lower than 5% the baseline values.

3. DISCUSSION OF RESULTS

3.1 Baseline Flow Characterization

As a first step of the study, baseline flow measurements, i.e., without operating the AFC system, were performed. The model was tested with both clean front surface and rough surface. For the rough configuration, two strips of Grit #60 elements were taped at the front side of the model. One strip was located upstream of the upper cylinder at the location of 0.68<y/H<0.85 and the other was located just upstream of the front-lower corner (0.00<y/H<0.0.16). The AFC openings, i.e., the suction holes and the PBS, were taped over in order to suppress passive disturbances.

3.1.1 Roughness Effects

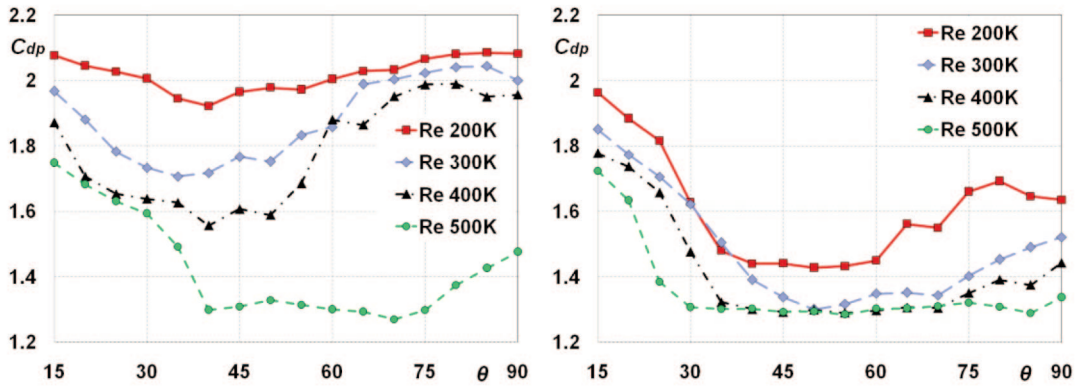

(a) Smooth (b) Rough

Figure 3. The form-drag coefficient, C_{dp}, plotted vs. the passive PBS location, θ, for various Reynolds numbers. The suctions holes and the PBS are taped over in order to minimize passive disturbances. a) Smooth surface without roughness. b) The front of the model rough, with Grit #60, to promote transition.

Figure 3 presents the form-drag coefficient (C_{dp}) vs. the PBS angle (θ) for both clean and rough surface conditions. It was expected that C_{dp} will not be highly sensitive to the PBS and the suction holes angle (θ) while they are taped over. Yet, it can be seen that C_{dp}, depending on the Reynolds number, is sensitive to the location of even covered openings of the AFC cylinder. The sensitivity is probably related to the fact that the tape has a certain degree of flexibility and two 0.05mm high steps at its upper and downstream ends, so it is not perfectly eliminating the passive effects of the AFC openings. For the smooth model the form-drag coefficient, C_{dp}, is more sensitive to θ as the Reynolds number increases. For Reynolds number of $2x10^5$, C_{dp} remains approximately around 1.9-2.1, in a good agreement to Hu's

study [9], which used a similar configuration but with both upper frontal and rear rounded corners, of R/H=0.157, at a significantly lower Reynolds number of 6,000. Increasing the Reynolds number causes significant reduction of C_{dp} for a wider range of θ locations. The minimum value of C_{dp} is obtained for Reynolds number of $5x10^5$ and is equal to about 1.3 at 40°<θ<75°. Munshi [10] studied the same configuration as Hu's but for R/H=0.135 and Reynolds number of 52k and measured drag coefficient of about 1.25. Note that our drag values are not corrected to the significant tunnel blockage of 20%. Since there is no reliable method for correcting Cp, we prefer not to correct the data. For future CFD studies it is recommended to simulate the model with the tunnel walls. A comment as to this effect was provided at the end of the experimental setup section.

Adding roughness to the front side of the model acts to promote transition so the drag coefficient for a certain range of θ is almost independent of the Reynolds number (Figure 3b). For all Reynolds numbers tested with the roughness, C_{dp} has a maximum value at PBS angle of θ=15°. The drag coefficient monotonically decreases as a consequence of increasing θ, until it reaches its minimal value for θ of 30° to 50°, depending on the Reynolds number. For θ>50°, the drag coefficients begin to increase again but up to a lower value than in the case of θ=15°.

3.1.2 The flow regime

In order to examine the reason for the observed changes of the drag coefficient, additional representative parameters of the flow should be considered. Figure 4 shows the variations of few integral non-dimensional parameters vs. the PBS angle, θ. The total pressure-drag coefficient, C_{dp}, for the current geometry, is the sum of two components $-C_{pb}$ (eq.1) and C_{df} (eq.2) defined as:

$$-C_{pb} = \frac{1}{H}\int_0^H \left(-C_{p,base}\right) dy \,;\ \text{for } x_{base}/H = 1 \tag{1}$$

$$C_{df} = \frac{1}{H}\int_0^H \left(-C_{p,front}\right) dy \,;\ \text{for } 0 < x_{front}/H < 0.127 \tag{2}$$

The wake width, ***d***, is defined as the vertical distance which includes the region where the velocity in the wake is less than 70% of the free-stream velocity. The Strouhal number, St is calculated from the dominant frequency observed by the wake unsteady pressure sensor, normalized by the model height ($St=f\cdot H/U_\infty$), while *St** is the same but this time normalized by the wake width, ***d*** ($St^*=f\cdot d/U_\infty$).

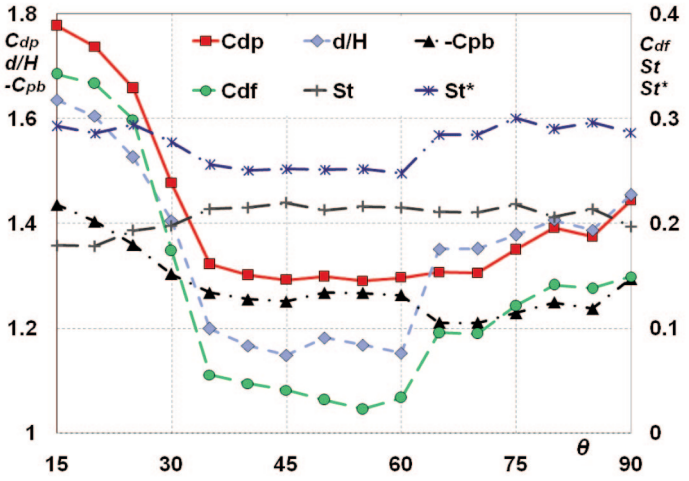

Figure 4. Integral non-dimensional parameters of the flow vs. PBS angle θ. Form-drag coefficient C_{dp}, the non-dimensional wake width d/H and the inverted base pressure,$-C_{pb}$. As defined in the text. The secondary axis on the right side refers to the coefficient of the form-drag contribution on the front side of the model, C_{df}, the non-dimensional dominant frequency measured in the wake, *St*, and *St** which is normalized by the wake length scale, *d*. The PBS and suction holes are taped. The front of the model is rough. $Re=4x10^5$.

Observing the data shown in Figure 4, up to PBS angle of θ =40°, all the parameters are monotonic with θ. With the reduction of Cdp, the wake width shrinks, the inverted base pressure - *Cpb* decreases and the Strouhal number (*St*) measured in the wake increases, all indicating drag reduction. For 40°<θ<60°, there is no significant change of the non-dimensional parameters. The trends change for θ>60°: While the drag coefficient remains about the same, the wake width *d/H* increases but the sub-pressure of the base decays. This fundamental change of the flow regime is also clearly seen in the *St** plot. The front-side drag coefficient and the inverted base pressure coefficient are the normalized forces acting on the front and rear surfaces of the model, respectively. The division of the total form-drag to its front and rear components allows distinguishing the reason for changes of the form-drag. Apparently these changes are a result of significant change in the flow regime around the model. In order to examine the flow structure, four representative conditions of PBS angles θ=15°,45°,75° and 90° are further considered.

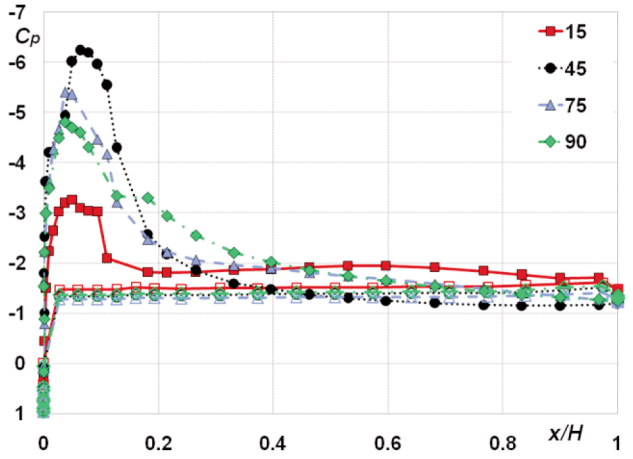

(a)

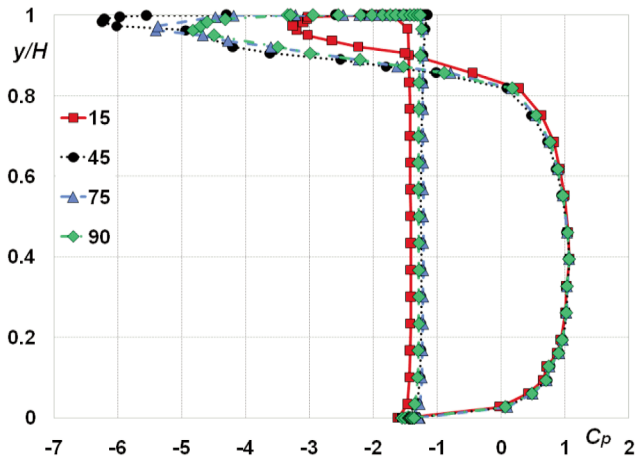

(b)

Figure 5. a) The mean pressure coefficient *Cp* vs. the normalized horizontal distance from the leading edge, *x/H*, for several PBS locations, θ, as indicated in the legend. The full symbols are for *y/H*>0.5. The empty symbols refer to the pressure taps where *y/H*<0.5. b) The mean pressure coefficient *Cp* vs. the normalized vertical distance *y/H*. Reynolds number *Re*=4x10^5, PBS and the suction holes are taped over, rough front surface.

The pressure distributions around the model vs. the horizontal and vertical axes are shown in Figure 5. For all PBS locations the flow near the lower surface of the model is completely separated. The flow is separated from the body surface right downstream of the sharp lower front edge with -1.5<*Cp*<-1.3. The pressure coefficient remains about the same up to the lower surface trailing edge. In contrast, the flow around the upper-curved-front surface could remain attached to the surface. For θ=15°, the flow on the upper rounded edge is accelerated in a relatively weak manner up to *Cp* value of about -3. Further downstream, *Cp* increases at the location of *x*/*H*=0.1 (note that currently *R*/*H*=0.127) and remains approximately the same up to the trailing edge of the model, indicating a separation bubble that is open to the wake. For θ=45° and θ=75°, the pressure monotonically increases (recovers) along the front upper side of the model, indicating that the flow is not necessarily separated and clearly unsteady. For PBS angle of θ=90°, the sudden break of the pressure recovery, for 0.1<*x*/*H*<0.2, indicates a separation bubble.

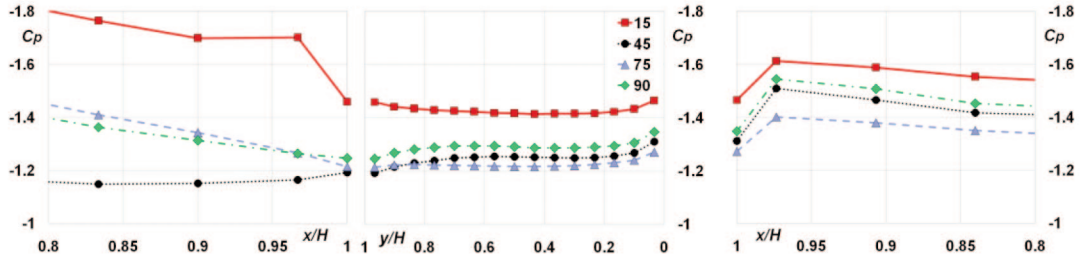

(a) Upper surface (b) Base pressure (c) Lower surface

Figure 6. Zoom-in on the mean pressure coefficient *Cp* of Figure 5. a) Upper surface *x*/*H*>0.8, *y*/*H*=1. b) Rear surface *x*/*H*=1. c) Lower surface *x*/*H*>0.8, *y*/*H*=0. In (a) and (c), *Cp* is plotted vs. *x*/*H* while in (b) *Cp* is plotted vs. y/H. Also in (c) x/H axis is inverted. The axes refer to Fig. 1b.

Figure 6 presents the *Cp* on the upper (a) and lower (c) surfaces just upstream of the wake formation region along with the pressure distribution on the rear surface of the model (b). Observing the pressure distribution vs. *y*/*H* (Figure 6b), it can be seen that the base pressure is uniform along most of the rear surface of the bluff-body model. The base pressure becomes more negative for PBS location of 15°, and increases with the following order: θ=90°, 45° and 75°. Figure 6c presents the pressure on the lower side of the model, where the forward edge is sharp, so the flow is separated and directly interacts with the wake. It is interesting to note that the pressure on the lower surface, just upstream of the rear side, is more negative than the base pressure but converges to its center region value quite rapidly. As for the rear side, *Cp* on the lower surface is more negative for θ=15°, and increases in the same order of θ=90°, 45° and 75°. This trend was not observed on the upper surface, where the front edge is curved. The pressure at the upper surface trailing edge region is identical for θ=45°,75° and 90°, while the corresponding base pressure is different. For PBS angle of 15°, where the flow on both surfaces of the body is separated, the difference between the pressures of the upper and lower surfaces is relatively small.

3.1.3 Unsteady aspects

Figure 7 and Figure 8 present the pressure spectra for several PBS locations. For all considered PBS locations there is a dominant peak in the wake pressure spectra, which is attributed to the vortex shedding phenomena. The dominant *St* number of the vortex shedding for θ=15° is around 0.18, it rises to a value of 0.21 for θ=45° and 75° and decreases to about 0.20 for θ=90°. These results are included in the St plot shown in Fig. 7. For the sensor placed on the model, there is a significant difference between the plots: For θ=45°and 90°, there is a dominant peak of the same frequency as in the wake. The flow that is attached to the body surface must separate at the rear-sharp corner. The sensor is located just upstream of this inevitable separation point, so it senses the alternating shear stress upstream of separation. For θ=15°, the pressure amplitude is significantly lower than for θ=45° and 90° and there is no clear dominant frequency to be observed in the model pressure spectra. This finding indicates that the shear layer that separates at the curved- front corner does not reattach, and a

separation bubble open to the wake exists. For θ=75° the magnitude of the dominant frequency, both on the model and in the wake, is relatively weak, in comparison to the wake sensor, but can still be identified. The variations indicated above are assumed to be linked to changes in transition and separation and no other parameter (such as minute changes in the open or taped over AFC openings.

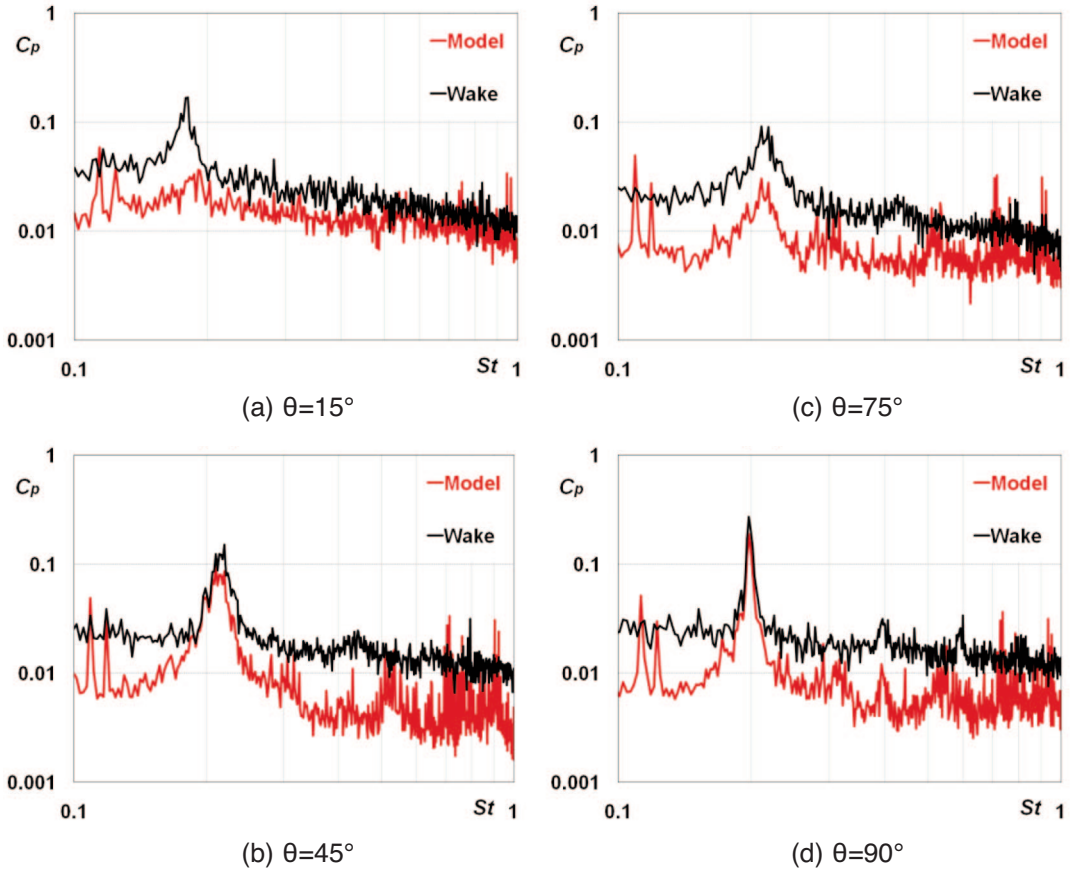

Figure 7. The pressure spectra measured at two locations: 'Model' – indicates the unsteady sensor on the upper trailing edge of the model (*x/H*=0.96 and *y/H*=1). 'Wake' - the upper unsteady sensor that is placed on the wake rake (*x/H*=4.13, *y/H*=1.46). PBS angles of 15°, 45°, 75° and 90°. Reynolds number 4x10^5, PBS and the suction holes are taped over, roughness of Grit #60.

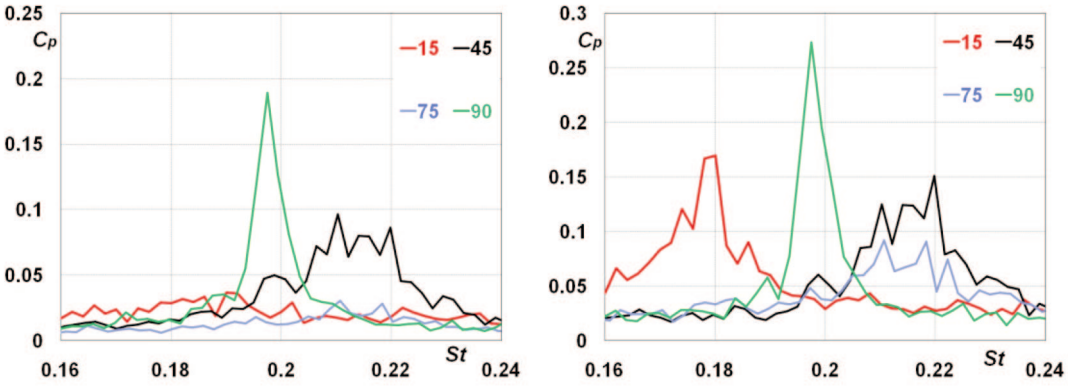

Figure 8. A limited frequency range of the pressure spectra, related to vortex shedding frequencies, shown in Figure 7 for several PBS locations (degrees) and sensor locations as mentioned in the legend. a) The unsteady Model sensor. b) The unsteady Wake sensor.

3.1.4 The wake

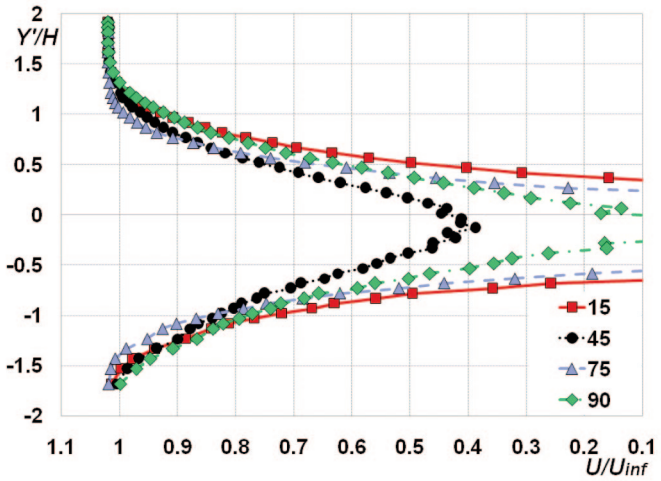

Figure 9. The distribution of the horizontal normalized x-velocity, U/U_∞, vs. the non-dimensional vertical location Y'/H, along the wake for PBS angles of 15°, 45°, 75° and 90°. The origin of the Y' axis is at the mid height of the bluff-body model (note that $Y'=y$-150 mm). Reynolds number Re=4x10^5, PBS and the suction holes are taped over, roughness of Grit #60.

Figure 9 presents the wake velocity distribution corresponding to the conditions of figures 5 and 7. Note that the reverse flow region is not presented since the measured velocity by the Pitot tube, oriented opposite the main direction to the free-stream flow, can not measure it. It can be seen that for θ=15°, where there is a separation bubble open to the wake on both the upper and lower surfaces, the wake is significantly wider than for the other PBS locations. Note also that for θ=45°, where the front-side drag coefficient is the lowest, but the base pressure is not at its maximal level, the wake minimal velocity is higher (about 0.4) than for the other PBS locations. Observing closely the wake structure, it can be seen that there is a correlation between the wake width, where fluid particles are more energetic (U/U_∞>0.9) and the corresponding base pressure results. The wake width for θ=75°, for this U/U_∞ range, is clearly narrower than the other PBS locations. Moreover, it seems that the wake width for θ=75°, at the range of U/U_∞>0.9, is narrower both on the upper side and on the lower side, where the separation bubble is open to the wake. For the other PBS locations, the wake width on the lower side, for U/U_∞>0.9, is approximately similar. Note that the total drag coefficient (CD) cannot be calculated from the wake velocity distribution because of the partly reversed flow in the wake.

3.2 SaOB Active Flow Control

The natural-uncontrolled state of the flow around a square prism with one round front edge was studied, analyzed and reported above. In this section wedescribe an attempt to manipulate the natural flow structure around the model using AFC. For the current study, the main mechanism was focused on delaying boundary layer separation from the front curved edge. For this purpose an array of 7 SaOB actuators was installed inside a cylinder that functions as the round-front-upper edge of the model. By that, the angle of the suction and pulsed blowing flow control openings can be altered ranging from PBS angle θ=15° to 90°. Another important parameter is the flow rate of the suction and pulsed blowing velocity that can be controlled by the supply pressure. The actuating magnitude is described here by the blowing momentum coefficient, as follows:

$$C_\mu = \frac{2h}{H}\left(\frac{u_b}{H}\right)^2\left(\frac{7}{15}\right) \tag{3}$$

Where h is the pulsed blowing slot width, H is the model's height, u_b the average blowing velocity, U_∞ the free-stream. In addition, C_μ is multiplied by 7/15 since there are for this configuration only

seven out of maximum of 15 SaOB actuators inside the FC cylinder [in 7, 8, 13 the details of the calibration procedure and results could be found].The suction velocity is about half of the mean pulsed blowing velocity [7,8,13], resulting in momentum that is quarter the pulsed blowing momentum. This effect is not included in the current calculations of the momentum coefficient. The frequency also increases with the inlet flow rate and pressure. The blowing and suction velocities are presented in a recent bench-top characterization of the actuator [7, 8, 13].

The model was tested with roughness elements of Grit #60 applied to the front side of the model.

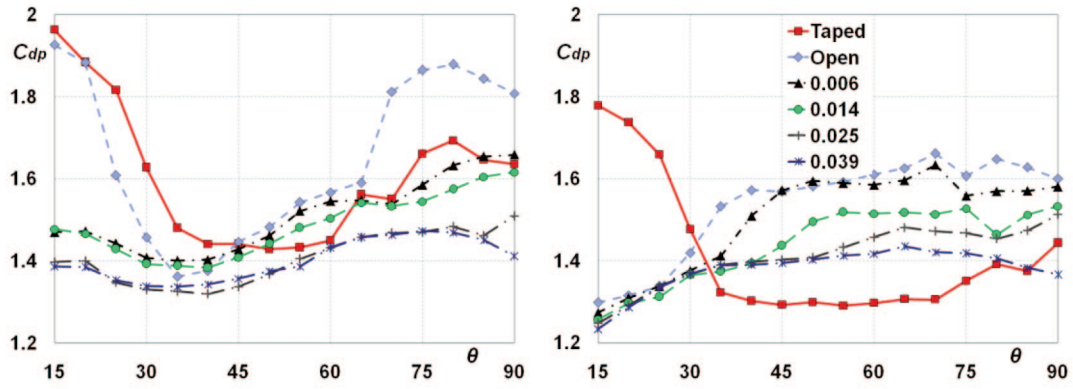

(a) Re 2x10^5 (b) Re 4x10^5

Figure 10. The form-drag coefficient (C_{dp}) plotted vs. the PBS location (θ) with different AFC configurations mentioned at the legend. The legend phrase 'Taped' refers to the configuration of taped over suction holes and PBS. 'Open' – is when the suction holes and PBS are exposed to the flow but without operating the AFC system. The legend numbers refers to the pulsed blowing momentum coefficients, C_μ (the normalized, by the free-stream pulsed blowing velocities u_j/U_∞, are 1.0, 1.5, 2.0 and 2.5, respectively). a) Re=2x10^5. b) Re=4x10^5.

The drag coefficient is plotted for two representative cases at Reynolds numbers 2 x10^5 and 4 x10^5. For Re=3 x10^5 and 5 x10^5, the C_{dp} distributions are quite similar to the case of Reynolds 400k (not shown). For Reynolds number of Re=2 x10^5, removing the tape from the PBS and suction openings has relatively small influence on the form-drag. The AFC for the cases where the baseline form-drag is high (i.e., 15°<θ<30°and 65°<θ<90°) is very effective so that it reduces C_{dp} to a low level of about 1.4. For Reynolds numbers higher than 2 x10^5, exposing the AFC cavities results in a dramatic change of C_{dp}. For small θ, C_{dp} drops from around 1.8 with taped openings to 1.3 with open exits. For higher θ, meaning that the slot is located further downstream, the trend is reversed such that the drag with open exits increases from 1.3 to around 1.6. The AFC effect is strongly linked to the flow regime when the actuators are not operated, i.e., as affecting laminar- turbulent transition. Munshi [10] made use of rotating cylinders at the upper-front and rear-edges of a square prism and reported a drag coefficient of about 0.6 in comparison to a baseline drag coefficient of about 1.25, for Reynolds number 52,000 and R/H=0.135. It should be noted that there are two AFC mechanisms involved: manipulating the boundary layer at the front curved edge and manipulating the wake formation region. Kubo [11] studied the effect of rotating cylinders at the front upper and lower edges with R/H=0.05, free-stream velocity of 6 m/sec and model height of 150 mm. It was found that for his baseline flow, the drag coefficient was about 2.5. Rotating one or both of the cylinders results in a decrease in the drag force, for optimal rotation velocities, yielding drag coefficients of 1.6-1.7. The normalized, by the free-stream, optimal rotation velocities are 1.0 for both cylinders and 1.4 when only one cylinder rotates.

As described above, and shown in Figure 10, the AFC is less effective and reacts monotonically, but weakly, for certain PBS locations where the baseline drag is already at a low level. On the other hand, it is highly effective and causes a strong response for other PBS locations, where the inevitable separation of the boundary layer, or perhaps to re-attach a separated shear-layer downstream, to the main separation at the aft of the body. This mechanism could force the vortices to form further

downstream, leading to an increase of the base pressure and reduced wake width. When the baseline flow is such that the boundary layers are not separated at the front surface, the efficiency of the AFC on the front-edge is limited for the reasons mentioned above.

3.2.1 Passive effects

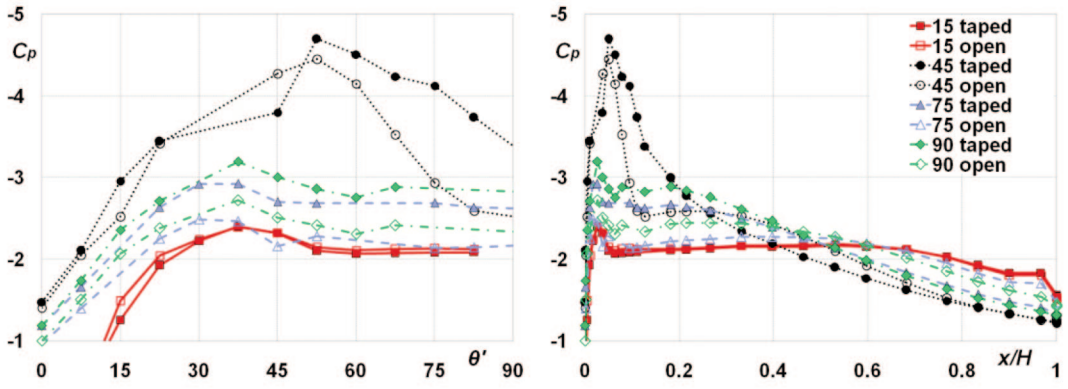

(a) (b)

Figure 11. a) The pressure distribution along the upper cylinder with θ' (note that θ' refers to the pressure tap angle and θ indicates the PBS location). b) The pressure distribution on the upper surface: C_p vs. x/H. The PBS angle θ is indicated at the legend. The legend phrase 'taped' refers to the configuration where the PBS and suction holes are taped- over, while 'open' is when the FC exits are exposed to the flow. Re=2 x10^5.

As described above (Figure 10a), for Re=2 x10^5, the passive effects of the FC exits on the drag coefficient were quite similar for both configurations of taped FC exits while they are exposed to the flow (i.e. 'open'). However, observing the data presented in Figure 11a, it can be noticed that the pressure distribution in not necessarily the same. For PBS location of θ=15°, the pressure distribution is quite similar. Separation takes place for both taped and open configurations around θ'=60° which is further downstream of the PBS. For PBS location of θ=45°, the passive effects are much stronger. The pressure distributes in a similar manner upstream the FC exits for both taped and open FC exits. Downstream of the PBS, a separation bubble is formed at the location of θ'=90° or x/H=0.127 for the open configuration while for the 'taped' configuration separation takes place at the aft of the model. The separation for the open configuration occurs downstream of the PBS (30° downstream of it). This finding implies that the effect of the AFC exits are also to interact with the external flow through the cylinder cavity (rather than only passive effects of transition). For PBS further downstream, PBS locations (θ=75° and 90°), it seems that the separation occurs upstream of the PBS at the same location for both configurations. However, the open AFC exits act to slightly decelerate the flow relative to the taped exits configuration. In addition, the separation bubble is longer with open AFC exits.

For Reynolds numbers higher than 2 x10^5 it would be reasonable to assume that the transition effects of the FC exits will be stronger. Figure 12 shows the pressure distributions on the upper surface for higher Reynolds number of Re=4 x10^5. These Reynolds numbers are roughly an order of magnitude lower than those of a full scale truck driving at 90km/h. It can be noticed for PBS of θ=15° that for taped AFC exits, the separation accrues at θ'=82° or x/H=0.11. The PBS is located upstream the separation point (θ=15° while θ'=82°). Therefore, exposing the FC exits to the flow acts to promote transition. As a result, the flow accelerates in a higher manner and the separation is delayed to the aft surface of the model. For PBS locations further downstream, the effect of the FC exits is similar to the case of Re=2 x10^5. It acts to separate the flow at x/H=0.127 or θ'=90°. This separation point is not coincidental. It is located where the upper cylinder and the main body surface merge. This connection is not perfectly smooth, therefore it creates a disturbance to the flow that could separate it.

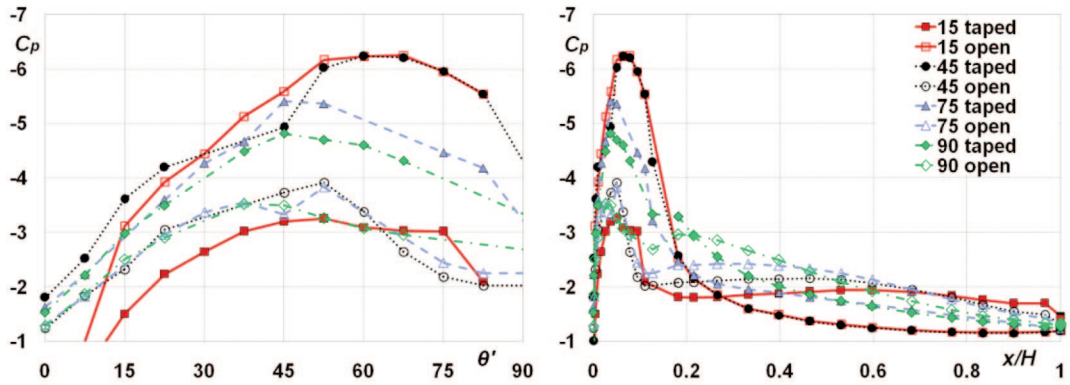

Figure 12. a) The pressure distribution along the upper cylinder plotted vs. θ' Over the AFC cylinder. b) Pressure distributions over the upper surface: C_p vs. x/H. The PBS angle θ is indicated at the legend. The legend phrase 'taped' refers to the configuration where the PBS and suction holes are taped-over, while 'open' is when the FC exits are exposed to the flow. Re= $4x10^5$.

3.2.2 Flow Control (FC) magnitude effect

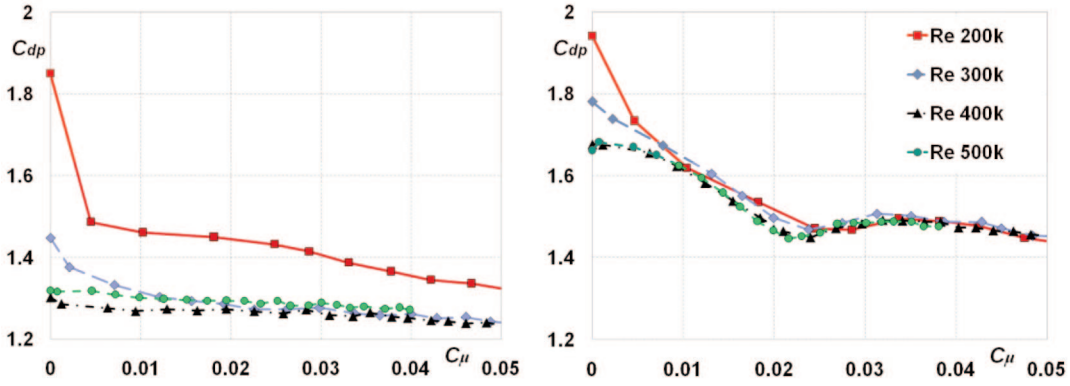

Figure 13. The effect of AFC magnitude: Form-drag vs. the normalized momentum coefficients. The Reynolds number is indicated in the legend. PBS and suction holes are open without operation the AFC are marked as C_μ=0. (a) θ=15°. (b) θ=75°.

Figure 13 shows sample results of the form-drag coefficient vs. the momentum coefficient for two PBS locations; of 15° and 75°. For θ=75°, with increasing AFC magnitude with a value of $C\mu$<0.01, the drag reduction responds quite weakly for Reynolds numbers of 4 $x10^5$-5 $x10^5$ and stronger for lower Reynolds number of 3 $x10^5$ and 2 $x10^5$. For 0.01<$C\mu$<0.02, the drag decreases significantly, from 1.6 to 1.45, regardless of the Reynolds number. For 0.02<$C\mu$<0.03 the drag slightly increases, indicating of a change of the AFC mechanism. Finally, for $C\mu$>0.03, C_{dp} decreases at a lower rate. Kubo [11] observed the same phenomenon of increment of the form- drag starting from a certain AFC magnitude (rotating cylinder speed in his case). It is encouraging to note the collapse of the data for different Reynolds numbers. Note also that the suction velocity is about half the mean pulsed blowing velocity, according to previous studies [8], so the integral results include effects of both the steady suction and the pulsed blowing in close proximity.

For PBS location of θ=15° and low Reynolds number of Re=2 $x10^5$, the drag is significantly reduced just for very low momentum magnitude. However, for higher Reynolds the baseline flow with open

AFC exits is significantly different, so C_{dp} is much lower and equals to about 1.3 for Reynolds numbers of 4 x10^5 and 5 x10^5. For these configurations, the effect of AFC magnitude is to monotonically reduce C_{dp} in a weak manner.

An additional insight for understanding the results could be achieved by considering the integral parameters (Figure 14). Observing the case of θ=75°, it can be seen that for low momentum coefficients ($C\mu$<0.005), the integral parameters are insensitive to the AFC magnitude. For 0.005<$C\mu$<0.02 all the parameters still behave in a manner similar to C_{dp}. While the value of C_{dp} decreases, the base pressure (C_{pb}), *Cl* and the *St* number (not shown) increase and the wake narrows. Both the front drag parameter C_{df} and the inverted base pressure -C_{pb}, are contributing to the total drag reduction. For $C\mu$>0.02, the trend seems to be different, indicating that different mechanisms become more significant. While the front drag parameter continues to decrease monotonically, the inverted base pressure increases, causing the total drag to increase as well. For $C\mu$>0.04, the base pressure converges to the baseline flow value, so eventually the total drag coefficient reduces only according to the front drag coefficient reduction. Note that the wake width, *d/H* and the *St* number (not shown) are insensitive to the above process (for $C\mu$>0.04), while the lift coefficient is proportional to the base pressure.

For θ=15°, the baseline C_{dp} value is already at a low level of 1.3 and therefore only weakly affected by the AFC. The base pressure, the lift coefficient and the *St* number are all hardly affected by the AFC. The wake width seems to slightly expand, probably because the addition of unsteady perturbation to the wake rather than a significant change in the flow structure around the model. The only parameter that changes is the front drag coefficient C_{df}, which is the cause to the reduction of the total drag. The baseline front drag coefficient, C_{df}, for θ=15° is about 0.03, much lower than the C_{df} of PBS location of θ=75°, which is about 0.3.

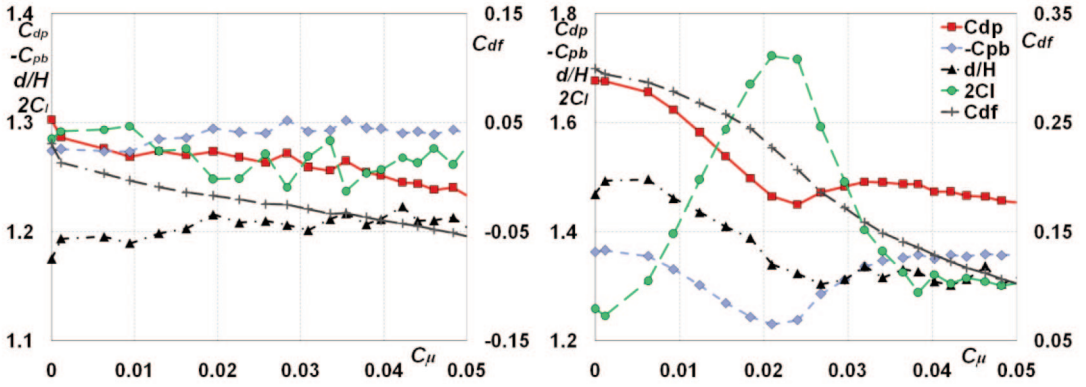

(a) θ=15° (b) θ=75°

Figure 14. A few integral parameters (as indicated in the legend) vs. the momentum coefficient: The form-drag coefficient, C_{dp}, the inverted base pressure, -C_{pb}, the non-dimensional wake width, *d/H* and the doubled lift coefficient, units of which are presented on the left side ordinate. The secondary axis is the contribution to the form-drag by the front edge of the model *Cdf*. Reynolds number is *Re*=4 x10^5. a) θ=15°. b) θ=75°.

Figure 15 shows the integral parameters of the flow vs. the momentum coefficient for *Re*=2 x10^5 at the same PBS locations as in Figure 14 (θ=15° and θ=75°). For θ=15°, the strong reduction of *Cdp* just for a low $C\mu$ comes together with a significant decrease of both the inverted base pressure and *Cdf*. In addition, the wake width shrinks and *Cl* increases (an indication of acceleration of the flow on the upper surface). For 0.005<$C\mu$<0.03, the inverted base pressure slightly increases, but C_{df} continues to decreases, so the total C_{dp} gradually reduce in a weak manner. The lift coefficient for this rage decreases, indicating that changes in the flow regime took place. For higher momentum coefficients ($C\mu$>0.03), both -C_{pb} and C_{df} decrease in a weak manner. As for the case of θ=75°, the flow behavior is similar to the case of *Re*=4 x10^5, described above (Figure 14b). However, unlike the case of *Re*=4 x10^5, where the asymptotic value of -C_{pb} was similar to the baseline value ($C\mu$=0), for *Re*=2 x10^5, the asymptotic value of -C_{pb} is lower than the case of $C\mu$=0.

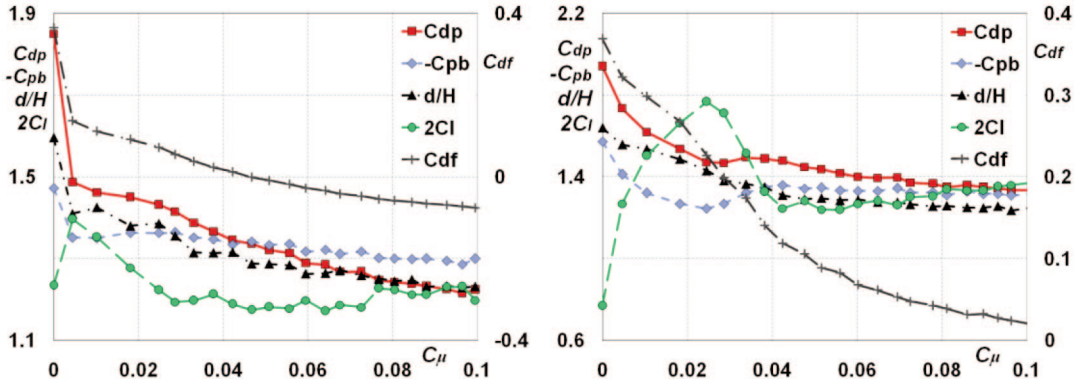

(a) θ=15° (b) θ=75°

Figure 15. A few integral parameters (as indicated in the legend) vs. the momentum coefficient: The form-drag coefficient, C_{dp}, the inverse of the base pressure, $-C_{pb}$, the non-dimensional wake width, d/H and the doubled lift coefficient. The secondary axis is the contribution to the form-drag by the front edge of the model C_{df}. Reynolds number is Re=2 x10^5. a) θ=15°; b) θ=75°.

More detailed information about the flow regime can be gained by observing the corresponding pressure distributions (presented in Figure 16). For θ=15° and Re=4 x10^5, where the integral parameters were almost insensitive to the AFC magnitude, the pressure distribution seems to be perfectly matched. The only difference is the acceleration at the PBS location leading to a lower pressure and the drag reduction related to this mechanism. For θ=75°, it can be seen that while $C\mu$=0.000, the pressure distribution accelerates in a relatively weak manner on the upper-rounded side of the model and thereafter separates of it. For $C\mu$=0.024, a major change in the flow regime is revealed. The separation takes place further downstream at x/H=0.127 or θ'=90° and a separation bubble is formed, such that the wake width becomes narrower and the base pressure increases. For higher blowing velocities, where the base pressure is more negative, the low pressure at the neighborhood of the PBS becomes more negative as well. The separation point is at the same location of θ'=90°, but it seems that the separation bubble shortens with increasing AFC magnitude above $C\mu$=0.024. Consequently, the pressure gradient recovery feature is also different for higher AFC magnitude. For all θ=75° cases, the pressure on the front side of the model is approximately the same, except on the upper-front edge as described above.

Figure 17 shows the pressure distribution for Re=2 x10^5. For C_μ=0.000, the flow on the upper surface accelerates in a weak manner and separates from the curved surface for both PBS locations of θ=15° and θ=75°. For θ=15°, the separation point is located at x/H=0.063 or θ'=60°. The AFC acts to accelerate the flow on the upper surface just for very low C_μ=0.004. Consequently, the separation from the upper curved edge is delayed. As a result, the inverted base pressure reduces significantly, C_l increases, C_{df} and d/H all decrease (Figure 15a). The effect of AFC for higher C_μ values is to accelerate the flow in a stronger manner. Consequently, the front drag coefficient gradually reduces with C_μ. Despite the upper surface acceleration, C_l decreases for 0.004<C_μ<0.028 (Figure 15a). This lift reduction is related to the decrease of both the base pressure and the pressure on the lower separated surface.

For θ=75°, the pressure distribution in quite similar to the case of Re=4 x10^5. The minimal inverted base pressure is obtained at C_μ=0.024, where a separation bubble takes place further downstream (θ'=90°). For higher C_μ values, the flow accelerated in a stronger manner so C_{df} decreases but the inverted base pressure increases.

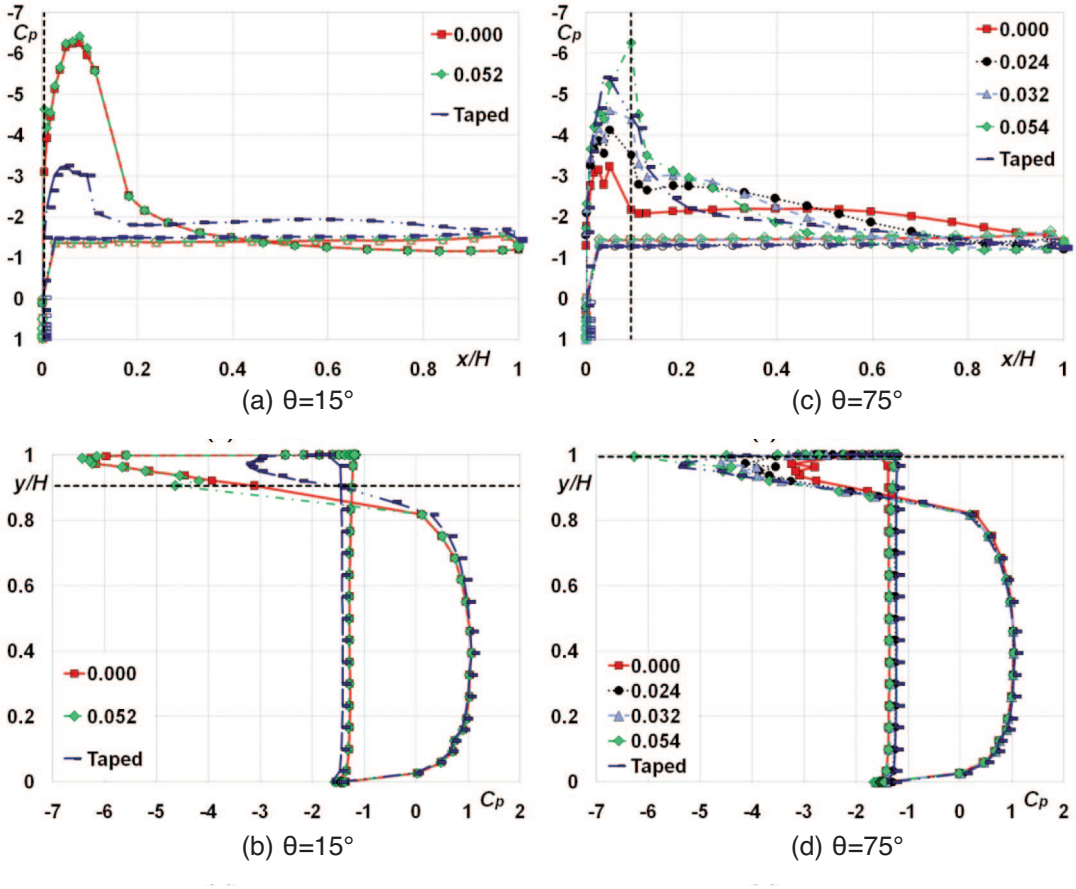

Figure 16. The mean pressure coefficient C_p vs. the normalized horizontal and vertical distances from the leading edge. Full symbols are for the upper surface, i.e. $y/H>0.5$. Empty symbols refer to the pressures measured at the lower surface, $y/H<0.5$. Reynolds number is $Re=4 \times 10^5$. The mean pulsed blowing momentum coefficient is shown in the legend. The case of taped AFC exits is also shown. For subfigures (a) and (b) the PBS angle $\theta=15°$, for (c) and (d) the PBS angle $\theta=75°$. Dashed lines indicate PBS location.

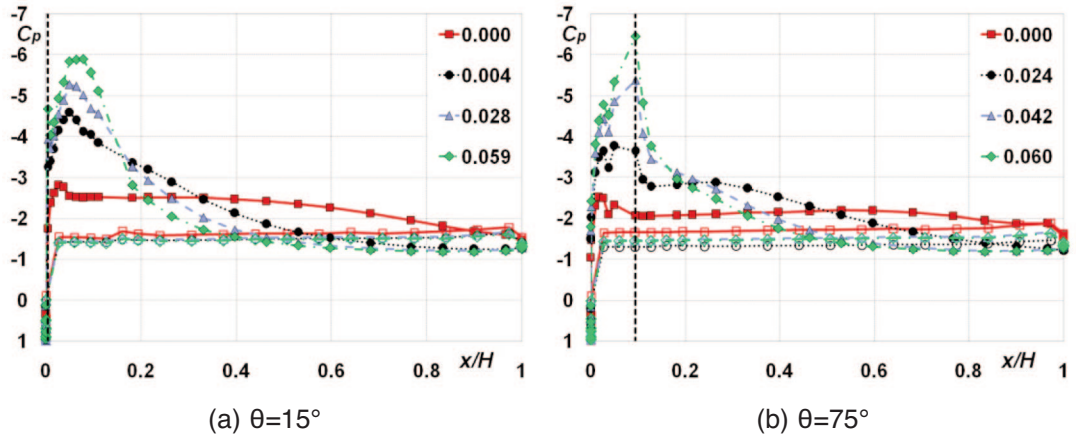

Figure 17. The mean pressure coefficient Cp vs. the normalized horizontal distances from the leading edge x/H. Full symbols are for the upper surface, i.e. $y/H>0.5$. Empty symbols are for the lower surface, $y/H<0.5$. Reynolds number is $Re=2 \times 10^5$. The blowing momentum coefficient is shown in the legend. a) $\theta=15°$. b) $\theta=75°$. Dashed lines indicate the PBS location.

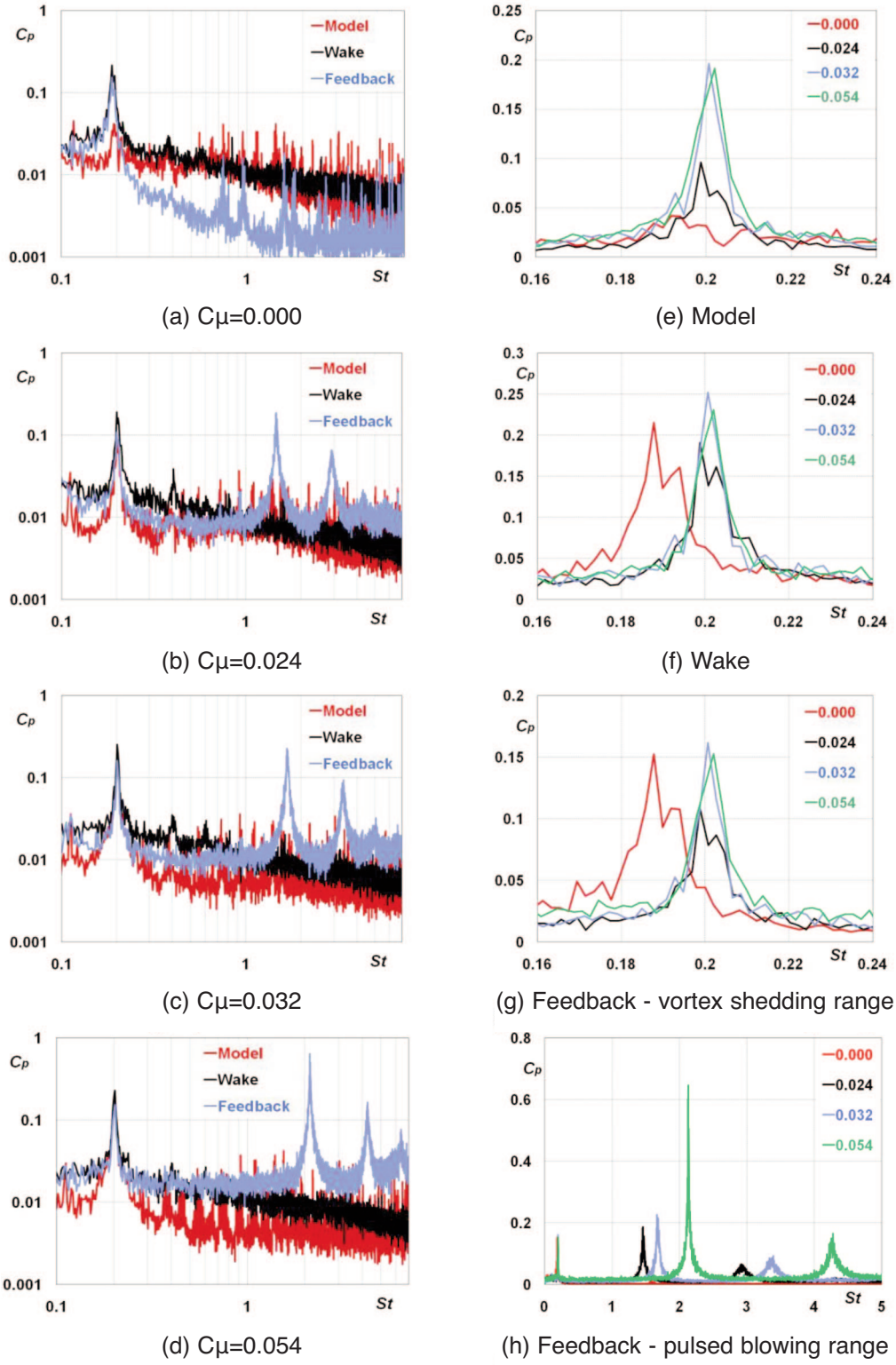

(a) Cμ=0.000

(e) Model

(b) Cμ=0.024

(f) Wake

(c) Cμ=0.032

(g) Feedback - vortex shedding range

(d) Cμ=0.054

(h) Feedback - pulsed blowing range

Figure 18. The pressure spectra for several AFC magnitudes of momentum coefficients: 0.000, 0.024, 0.032 and 0.054. *Re*=4 x10^5, θ=75°. The three locations are indicated in the legend: Model - the unsteady pressure sensor is located on the upper trailing edge (x/H=0.96 and y/H=1). Wake- the unsteady sensor is located on the wake rake (x/H=4.13, y/H=1.46). (h) SaOB Feedback tube – unsteady pressure sensor located in the middle actuator control port for measuring pulsed blowing frequency and external flow oscillations as well.

As mention above, the location where x/H=0.127 or θ'=90° is a potential separation point due to the discontinuity arising from the connecting between the cylinder to the upper model surface. Therefore, there might be some unsteady separation bubbles that are being formed at this location. This phenomenon could not always be observed by the average pressure distribution. For example, at PBS location of θ=15° and Re=2 x10^5, the inverted pressure is lower for C_μ=0.004 than C_μ=0.028 (Figure 15a). However, there is no outward differences between their pressure distribution expect the stronger acceleration for C_μ=0.028 (Figure 17a). A possible explanation for this conflict is that some short unsteady separation bubbles are being formed. These bubbles cannot be observed by the pressure distribution. As mentioned above (Figure 16c), the separation bubble length has a major effect on the base pressure, which might be the explanation for this behavior. In a similar manner, for PBS location of θ=75°, there might be separation bubbles that are being formed for C_μ=0.042 and 0.060 at the location of θ'=90° (Figure 17b). This could explain the increase of -C_{pb} relative to C_μ=0.024, since the inverted base pressure decreases with the separation bubble length when formed at the same location of θ'=90° (Figure 16c).

Figure 18 shows the pressure spectra for Re=4 x10^5 with the PBS at θ=75°. For the baseline flow with open exits (C_μ=0.000), where the flow is separated more upstream, the pressure spectra peak for the model unsteady sensor is relatively weak. The normalized frequency of the vortex shedding for this case, as measured by the wake sensor is around St=0.19. For the Feedback tube unsteady sensor, there is a dominant peak at the same frequency of the vortex shedding. This finding is consistent with Figure 16 which shows a separation at the location of the PBS. Activating the AFC results an increase of the vortex shedding frequency to St=0.20. The same frequency is measured on both the Model and Feedback sensors. It is interesting to note that Strouhal number for C_μ=0.032 and 0.054 is greater than the baseline flow case (C_μ=0.000), indicating drag reduction, but the base pressure values are similar. On the other hand, for AFC magnitude of C_μ=0.024, the Strouhal number is the same as for higher C_μ values, but the inverted base pressure is smaller. This finding implies that St is more related to the total drag force. However, the peak magnitude of the pressure oscillations at the vortex shedding frequency can imply some other differences in the flow structure. The Model's pressure spectra show the same peak magnitude for C_μ=0.032 and 0.054. On the other hand the peak for C_μ=0.024, where the inverted base pressure was minimal, is weaker. For the Wake and Feedback sensors the trend is similar but with smaller differences.

Additional parameter which affects the AFC efficiency is the pulsed blowing frequency. For a circular cylinder with an array of SaOB actuator, it was found that the maximal drag reduction is achieved at Strouhal number twice the natural vortex shedding [8]. The pulsed blowing frequency, for a given array of SaOB actuators, increases with the pressure supply and the mean blowing velocity, as can be seen from Figure 18h. This could be one of the reasons for the trends mismatch between the Strouhal number and the base pressure. Note however that the current range of excitation frequencies is almost an order magnitude higher than the natural vortex shedding frequency of the square prism.

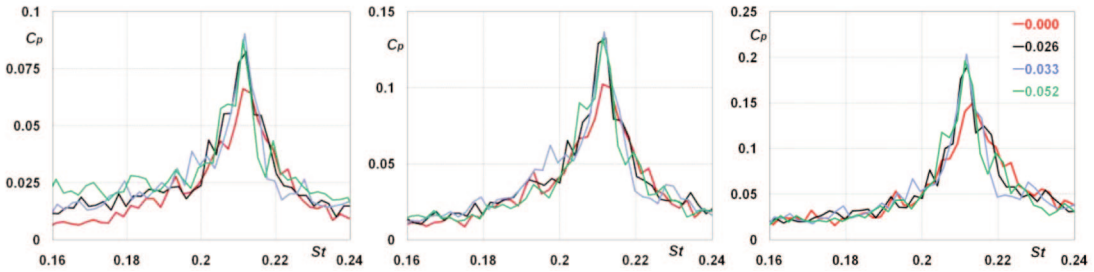

(a) Feedback (b) Model (c) Wake

Figure 19. The pressure spectra for several AFC momentum coefficients mentioned at the legend. Reynolds number is Re=4 x10^5, θ=15°. a) SaOB feedback tube sensor -located in the middle actuator control port. b) Model sensor- located on the upper trailing edge of the model surface x/H=0.96 and y/H=1. c) Wake sensor- located on the wake rake (x/H=4.13, y/H=1.46).

For PBS angle of θ=15° (Figure 19), the base pressure is insensitive to the AFC magnitude. The pressure spectra are almost identical for the baseline flow and with activating the AFC. For all of the dynamic sensors there is a dominant peak with a Strouhal number of about St=0.21. The magnitude is higher with AFC operating, but St is insensitive to the AFC magnitude. The AFC accelerates the flow around the cylinder, thinning the boundary layer, increasing the skin friction and the magnitude of the vortex shedding downstream of the cylinder.

In comparison to PBS locations of θ=75° the Strouhal number is slightly higher. We find a similarity of the pressure spectra magnitude for this case and the optimal case of θ=75° (C_μ=0.024). Note that the pressure spectra magnitudes for PBS angle of 15° and for the optimal case of PBS θ=75° (C_μ=0.024) are all weaker than the other AFC magnitude of θ=75°. This statement excludes the Model sensor magnitude with the configuration of θ=75° and C_μ=0.000 where the flow is separated.

3.2.3 Energy efficiency

One of the main goals of the current study is to investigate the effect of AFC on the drag force, as active flow control tool considering the overall energy efficiency. In order to quantify this aspect, and to compare it to different AFC systems, the dimensionless drag coefficients were multiplißed by the dynamic pressure, by the reference area and by the free-stream velocity to define the reference power required to overcome the drag. These values assisted to define an energy figure of merit, AFM4 as follows [8]:

$$AFM4 = \frac{W_{d0}}{W_d + W_a} \tag{4}$$

$$W_d = qU_\infty AC_{dp} = 0.5\rho U_\infty^3 bHC_{dp} \tag{5}$$

Where W_d is the power required to overcome the drag with the presence of AFC, W_{d0} is the power required to overcome the baseline drag (exposing the AFC exits to the flow but without operating the AFC system) and W_a is the actuation power, i.e., the power consumed by the actuators' array [8]. The free-stream dynamic pressure is indicated by q. All measured performance data points with $AFM4$>1 indicate increased system energy efficiency. The relationship between the actuation power and the free-stream velocity is established through the power coefficient:

$$C_{pwr} = \frac{W_a}{qU_\infty bH} = \frac{W_a}{0.5\rho U_\infty^3 bH} \tag{6}$$

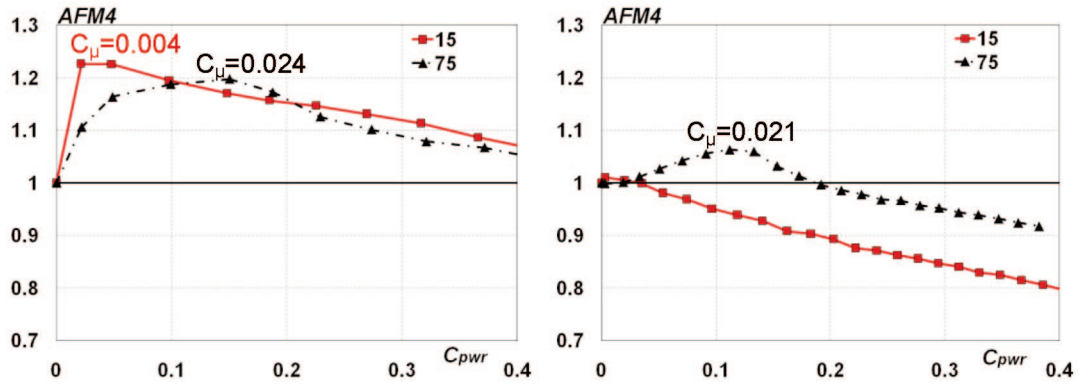

(a) Re=2 x10^5 (b) Re=4 x10^5

Figure 20. Energetic efficiency, AFM4 for two PBS locations, θ, as indicated at the legend. The C_μ values where the AFM4 is maximal are indicated in the figures. (a) Re=2 x10^5. (b) Re=4 x10^5

The AFM4 plot is shown in Figure 20, for two PBS locations of θ=15° and 75°, at Reynolds numbers of 2 x10^5 and 4 x10^5. It should be noted that for each scan (or AFM4 curve), the free stream velocity that was used in order to calculate the AFM4 and C_{pwr} parameters is the average velocity of the entire scan. The reason for the above is that the AFM4 and C_{pwr} parameters are very sensitive to minor changes in the free-stream velocity since U_∞ is cubic in Eq. 6.

Observing Figure 20a, which is the case of Re=2 x10^5, it can be noticed that the AFC is energetic efficient for C_{pwr}<0.4 for both PBS location of θ=15° and 75°. This high efficiency is related to the base flow of this case which is massively separated. The AFC on the front side, affects the flow in two manners. First, by accelerating the flow on the front curved edge, leading to lower pressure on average on the front side of the model (or lower C_{df}). Second, the AFC acts to delay the separation, leading to higher pressure on the rear side of the model (or lower -C_{pb}). For Re=4 x10^5 (Figure 20b), the *AFM4* parameter is greater than one only for θ=75°. The most efficient operating point is where C_{pwr}=0.11 or C_μ=0.021. This operation point is where the inverted base pressure obtained its lowest value (Figure 14b).

3.3 Model incidence sensitivity

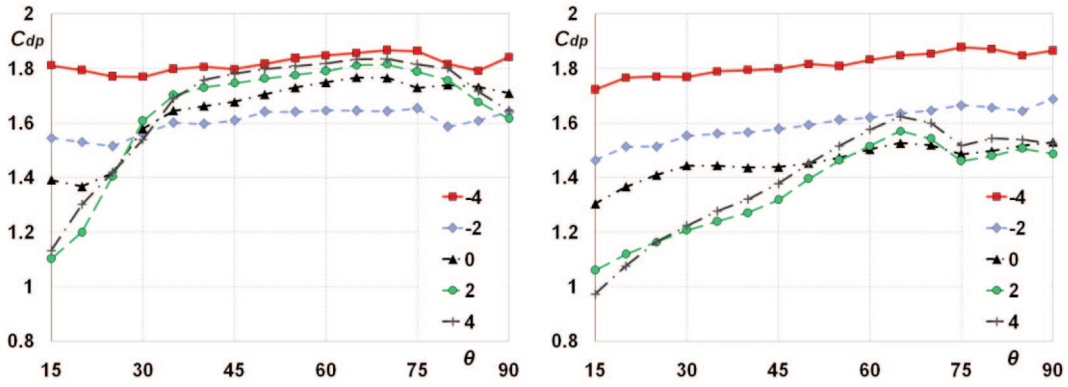

(a) C_μ=0.000 (b) C_μ=0.025

Figure 21. The form-drag coefficient, C_{dp}, plotted vs. the PBS location, θ, for various angles of attack as mentioned at the legend. The front of the model is rough, with Grit #60. Re=4 x10^5. a) FC exits (Suction holes and PBS) are exposed to the flow without pressure supply (C_μ=0). b) AFC is activated C_μ=0.025 (u_b/U_∞=2.0).

For most of the study, the model angle of attack was set to zero. Nevertheless, the angle of attack (α) is an important parameter when considering AFC application. Currently, only a narrow range of incidence angles was checked, in-line with the common range of side-wind directions for heavy vehicles operating at highway permitted speeds. The effect of α on the pressure drag coefficient is shown in Figure 21. The positive direction of α is clockwise. For α=-4°, the drag coefficient is only weakly affected by the PBS location. When the FC exits are exposed to the flow without pressure supply (C_μ=0), C_{dp} value is about 1.8 independent of the PBS location. The operation of AFC does not yield drag reduction. The drag slightly increases with θ (Figure 21b). This trend is similar for α=-2°. However, the average C_{dp} value for this case is around 1.6. For zero or positive angles of attack, the trend is different. The passive effects of FC exits (Figure 21a) act to reduce C_{dp} significantly for PBS location of θ=15°. For α=2° and 4°, C_{dp} is even lower. For PBS locations further downstream, the drag coefficient increases. For this rage of α=0°, 2° and 4°, the effect of AFC is to reduce C_{dp} even more for all PBS locations. This behavior is related to the asymmetric shape of the model, which its lower front corner is sharp while the opposite, upper- front edge is rounded.

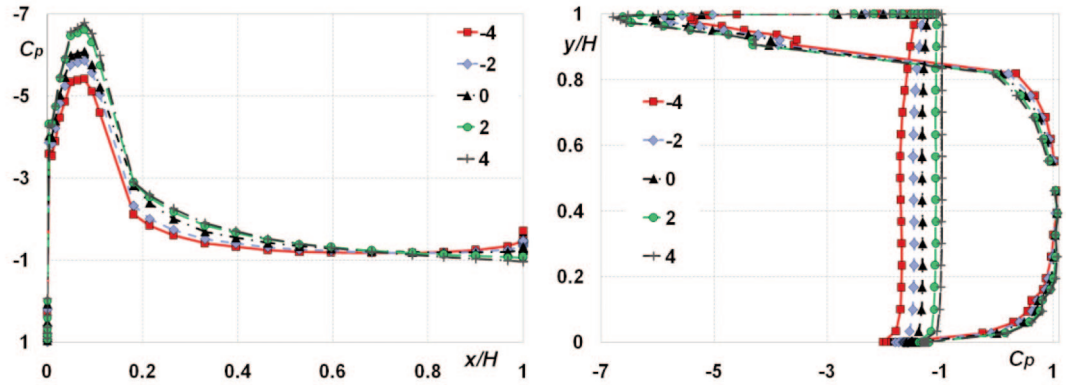

Figure 22. The pressure distribution for various angles of attack as mentioned at the legend. The PBS location is θ=15°, with blowing magnitude of C_μ=0.025. *Re*=4 x10^5. The front of the model was roughened, with Grit #60. a) C_p vs *x/H* of the upper surface. b) C_p vs. *y/H*.

As seen earlier, for PBS location of θ=15°, the AFC exits affect the flow in a strong manner. It acts to strongly accelerate the flow and delay the separation to the rear-edge of the upper surface with or without pressure supply (Figure 16a). This trend is similar for the other angles of attack that have been tested. Observing Figure 22a, it can be noted that for all tested α, the flow on the upper surface is also highly accelerated. The rear side of the model is separated and characterized by uniform pressure. The base pressure is the lowest for α=-4° and increases with α (Figure 22b). The effect of α on a square prism with sharp edges was studied by Lee [12] that attributed the changes in the flow to the shear layers interaction with the body's surface. It would be reasonable to assume that the same mechanisms are involved for the current study. As α is increased, the separated shear-layers beneath the lower surface alternately reattach to the rear corner. As a result, the shear layers, which for negative α left the prism at the front corner, now leave it at the rear corner. Thus, the formation region moves downstream and the base pressure increases [12]. It should be noted that the pressure distributions are the time average values therefore this phenomenon cannot be observed in the data shown in Figure 22.

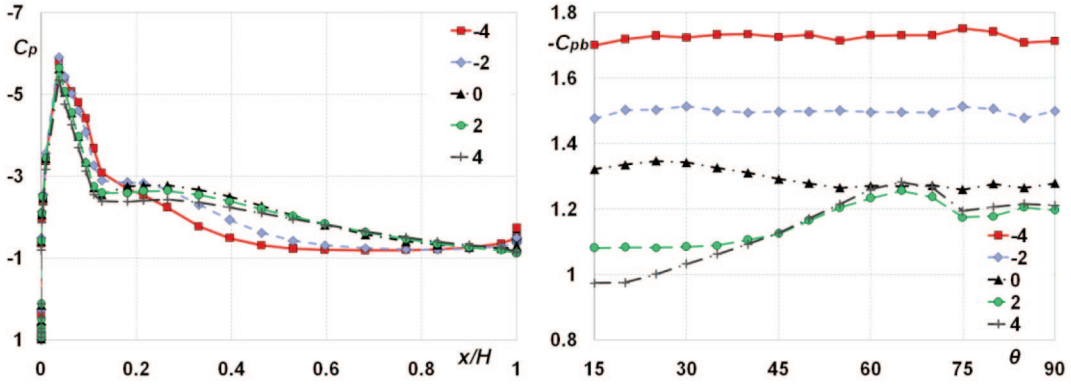

Figure 23. a) *Cp* vs. *x/H* (upper surface) for PBS location of θ=45°. b) The inverted base pressure, -*Cpb*, vs. the PBS location, θ. The plots are shown for various angles of attack (Deg.) as mentioned at the legend. C_μ =0.025. *Re*=4 x10^5. The front of the model is rough.

The pressure distributions are also shown for another PBS location of θ=45°. For this configuration, the effect of AFC for α=0° is to accelerate the flow and to create a separation bubble (Figure 23a). Reducing the angle of attack (more negative) acts to shrink the bubble length (same explanation as described above). It is interesting to note that despite the differences between the pressure distributions

for θ=15° and 45°, the inverted base pressure is identical when α<0°. This trend is not observed for α>0° (Figure 23b).

4. CONCLUSIONS

An experimental study of a square prism model with an AFC cylinder placed at the front-upper edge was performed and described. A Baseline flow characterization was made, investigating the device passive effects on the flow regimes and resulting structure. The AFC parameters that were tested include suction and pulsed blowing magnitude, actuation position along the upper-curved-edge, angle of attack and oscillation frequency of the actuators. An attempt was made to document AFC effects and understand the flow mechanism enabling the significant performance alternations using static and dynamic pressure data. The suction and oscillatory blowing applied at the front curved edge was found to be capable of preventing separation from the front-curved edge, reducing the drag force and narrowing the wake in an energy efficient manner, for certain conditions. The favorable effects of AFC are maintained also with simulated side-winds, currently via model angle of attack varation, mainly with PBS locations smaller than 45 deg. Further study is underway, focusing on a symmetric bluff-body with AFC activation on one or both of the front curved edges, trying to isolate the suction from pulsed blowing mechanism of the SaOB actuator.

ACKNOWLEDGEMENTS

This project was partially supported by The Rinna Bolle Student Travel Fund of Tel Aviv University. Additionally, the authors would like to acknowledge support provided to this project by our International partners Mr. Linus Hjelm of Volvo Trucks and Mr. Oz Shamia of AFC Tech., Israel. The support of TAU Meadow Aerolab members: Vitali Palei,Victor Troshin, Ori Friedland, Dima Sarkorov, Danny Dolgopyat, Artur Minasyan, Nir Morgolis and Nir Modanis is appreciated. Members of the Technical staff, lead by Mr. Shlomo Pasteur: Eli, Kronish, Avraham Blas, Shlomo Moshel, Shlomi Blaivis, Tomer Bachar and Mark Vassermann enabled this project. Partial financial support by the Meadow fund is appreciated.

REFERENCES

[1] Hucho, W.H., *Aerodynamics of road vehicles: from fluid mechanics to vehicle engineering*, edited by Wolf- Heinrich Hucho; contributors, Syed R. Ahmed ... [et al.], ed. W.-H. Hucho and S.R. Ahmed. 1987, London, Boston, Butterworths.

[2] Roshko, A., Perspectives on bluff body aerodynamics. *Journal of Wind Engineering and Industrial Aerodynamics*, 1993. 49(1-3): p. 79-100.

[3] Choi, H., W.-P. Jeon, and J. Kim, Control of Flow Over a Bluff Body. *Annual Review of Fluid Mechanics*, 2008. 40(1): p. 113-139.

[4] Arwatz, G., Fono, I., and Seifert, A., Suction and Oscillatory Blowing Actuator. *AIAA Journal*, 2006. 46(5): p. 1107-1117.

[5] Seifert, A., Stalnov, O., Sperber, D., Arwatz, G., Palei. V., David, S., Dayan, I., Fono, I., *Large Trucks Drag Reduction Using Active Flow Control*. AIAA paper 2008-743.

[6] Seifert, A., Dayan, I., Horrell, C., Grossmann, J. and Smith, A., *Heavy Trucks Fuel Savings using the SaOB Actuator, in Aerodynamics of Heavy Vehicles III: Trucks, Buses and Trains*, G.A.C.. Dillmann, Editor. 2010: Potsdam, Germany.

[7] Shtendel, T. and Seifert, A., "Three-dimensional Aspects of bluff-body drag reduction by active flow control", *Int. J. Heat and Flow*, Volume 45, February 2014, Pages 109–127.

[8] Shtendel, T., Fundamentals of bluff body drag reduction by active flow control. M.Sc. thesis, Tel Aviv University, 2012.

[9] Hu, J.C. and Y. Zhou, Aerodynamic Characteristics of Asymmetric Bluff Bodies. *Journal of Fluids Engineering*, 2009. 131(1): p. 011206.

[10] Munshi, S.R., V.J. Modi, and T. Yokomizo, Fluid dynamics of flat plates and rectangular prisms in the presence of moving surface boundary-layer control. *Journal of Wind Engineering and Industrial Aerodynamics*, 1999. 79(1–2): p. 37-60.

[11] Kubo, Y., et al., On the suppression of aerodynamic instabilities through the moving surface boundary-layer control. *Journal of Wind Engineering and Industrial Aerodynamics*, 1992. 41(1–3): p. 205-216.

[12] Lee, B.E., The effect of turbulence on the surface pressure field of a square prism. *Journal of Fluid Mechanics*, 1975. 69: p. 263-282.

[13] Wilson, J., Schatzmann, D., Arad, A., Seifert, A. and Shtendel, "Suction and Pulsed-Blowing Flow Control Applied to an Axisymmetric Body", *AIAA Journal*: 1-15, 10.2514/1.J052333, Posted online on 6 Aug 2013.